

A Multimodal Learning Framework for Comprehensive 3D Mineral Prospectivity Modeling with Jointly Learned Structure-Fluid Relationships

1st Yang Zheng

*School of Geosciences and Info-Physics
Central South University*
Changsha, People's Republic of China
yang.zheng2@ucalgary.ca

2nd Hao Deng

*School of Geosciences and Info-Physics
Central South University*
Changsha, People's Republic of China
Corresponding author: haodeng@csu.edu.cn

3rd Ruisheng Wang

*Department of Geomatics Engineering
University of Calgary*
Calgary, Canada
ruiswang@ucalgary.ca

4th Jingjie Wu

*School of Geosciences and Info-Physics
Central South University*
Changsha, People's Republic of China
225012198@csu.edu.cn

Abstract—This study presents a novel multimodal fusion model for three-dimensional mineral prospectivity mapping (3D MPM), effectively integrating structural and fluid information through a deep network architecture. Leveraging Convolutional Neural Networks (CNN) and Multilayer Perceptrons (MLP), the model employs canonical correlation analysis (CCA) to align and fuse multimodal features. Rigorous evaluation on the Jiaojia gold deposit dataset demonstrates the model's superior performance in distinguishing ore-bearing instances and predicting mineral prospectivity, outperforming other models in result analyses. Ablation studies further reveal the benefits of joint feature utilization and CCA incorporation. This research not only advances mineral prospectivity modeling but also highlights the pivotal role of data integration and feature alignment for enhanced exploration decision-making.

Keywords—component—multimodal learning, 3D MPM, geological data integration, canonical correlation analysis, mineral deposit distribution

I. INTRODUCTION

Mineral prospectivity modeling (MPM) is a crucial tool in the field of geoscience, aiming to predict the distribution of mineral deposits based on various geological, geophysical, and geochemical data. With the advancement of technology and the availability of diverse data sources, the accuracy and comprehensiveness of MPM have improved significantly [1]–[7].

Three-dimensional mineral prospectivity modeling (3D MPM) offers the capability to quantitatively and visually predict mineral prospectivity at a deposit scale, integrating predictor variables from multiple domains and associating them with mineralization, which can lead to information discrepancies due to the distinct properties of these data types [8]–[15]. However, the integration of heterogeneous data types, such as 3D structural and fluid data, remains a challenge due to their distinct natures and information discrepancies. The

high complexity and variability among structural and fluid data further complicate the task of integration [16]–[20].

In this work, we aim to address these challenges and improve the accuracy of 3D MPM by introducing a novel approach based on Canonical Correlation Analysis (CCA). Our main objectives are to introduce CCA as a tool to capture correlations between multiple modalities, thereby enhancing the accuracy of mineral prospectivity predictions, and to deepen our understanding of the geological processes that govern mineral deposit distribution. By maximizing the correlation between these data modalities, we intend to capture the underlying relationships that contribute to accurate mineral prospectivity modeling. Through this approach, we can effectively address the challenges posed by the integration of diverse data types and provide a comprehensive understanding of the geological processes underlying mineral deposit distribution.

II. RELATED WORKS

The field of mineral prospectivity modeling has seen significant advancements, driven by the increasing availability of diverse data sources and advanced modeling techniques.

A. Mineral Prospectivity Modeling

Traditional mineral prospectivity modeling methods have primarily relied on geological, geophysical, and geochemical data to predict mineral deposit distributions. These methods can be broadly categorized into two main approaches: knowledge-driven [2] and data-driven [1], [3]–[7] methods. While these approaches have shown promise, they often struggle to handle the complexity and variability of 3D data.

B. Three-Dimensional Mineral Prospectivity Modeling (3D MPM)

3D MPM has emerged as a powerful technique for predicting mineral deposits at a deposit scale. It leverages 3D geological models and integrates predictor variables from multiple domains. This approach offers the potential for accurate and comprehensive predictions but introduces challenges related to the integration of heterogeneous data types [8]–[15].

C. Multimodal Fusion in Geological Modeling

The integration of multimodal data in geological modeling has gained attention as researchers seek to improve the accuracy and effectiveness of mineral prospectivity predictions. Previous work has explored the fusion of geological and geophysical data [21]–[23], geophysical and remote sensing data [24], and geological and geochemical data [21]. These studies have demonstrated the potential benefits of combining diverse data sources for enhanced modeling outcomes.

D. Canonical Correlation Analysis (CCA)

Canonical correlation analysis is a statistical method used to explore and quantify relationships between two sets of variables. It has found applications in various fields, including image analysis, genetics, and natural language processing [25]. The goal of CCA is to find a linear transformation of two sets of variables that maximizes their correlation [26]. In deep learning, this can be used to find a low-dimensional representation of two sets of neural network activations that are highly correlated [27]–[30].

E. Our Contribution

In this study, we build upon the advancements in mineral prospectivity modeling, 3D MPM, multimodal fusion, CCA, and deep learning techniques to propose a novel approach. Our approach leverages CCA to align and fuse structural and fluid data within a shared feature space, facilitating enhanced mineral prospectivity predictions. By integrating these diverse data modalities, our method addresses the challenges posed by information discrepancies and variability, ultimately contributing to the field’s understanding of geological processes governing mineral deposit distribution.

III. METHODOLOGY

A. Problem Definitions

Suppose that we are given mineralization information data with N samples for training, corresponding with their ore-bearing properties. One training sample can be denoted as the following tuple:

$$(\mathbf{x}_n^s, \mathbf{x}_n^f; y_n), n = 1, \dots, N$$

where $\mathbf{x}_n^s \in \mathbf{X}^s$ and $\mathbf{x}_n^f \in \mathbf{X}^f$ stand for structure and fluid representations of the n -th sample respectively, whereas y_n denotes the corresponding label with $y_n = 1$ if the n -th sample is ore-bearing or non-ore-bearing otherwise. We aim to perform multimodal prospectivity modeling by jointly learning the relationships between structure and fluid data, so we build

two feature maps f and g for shape descriptors and fluid properties respectively. The challenge is to effectively combine these multiple sources of information to conduct more comprehensive and robust predictions about the distribution of mineral deposits.

B. Multimodal Learning Network

The proposed network consists of two feature extraction branches, one for structural and one for fluid features. The structural branch is an extension of the convolutional neural network (CNN) $f(\mathbf{x}^s)$, which takes projected images of 3D geological models as input and learns features associated with mineralization from the images. This branch is based on our previous work of [13] for 3DMPM. The fluid branch is implemented with a multilayer perceptron (MLP) $g(\mathbf{x}^f)$ to model the relationships between mineral deposits and fluid properties, which represent complex nonlinear processes. The latent features extracted by the two branches are blended by a fusion layer

$$\mathbf{a}_F = \sigma(\mathbf{W}_{F-1}[f(\mathbf{x}_n^s), g(\mathbf{x}_n^f)] + \mathbf{b}_{F-1}) \quad (1)$$

where \mathbf{W}_{F-1} and \mathbf{b}_{F-1} are the parameters of the fusion layer, F is the index of the fusion layer, and σ is the activation function. The blended features \mathbf{a}_F are then put through a transition layer to transform them into a format suitable for final classification. The output probability $p(\tilde{y}_n | \mathbf{x}_n^s, \mathbf{x}_n^f)$ is computed using another layer with parameters \mathbf{W}_{F+1} and \mathbf{b}_{F+1} as follows:

$$p(\tilde{y}_n | \mathbf{x}_n^s, \mathbf{x}_n^f) = \sigma(\mathbf{W}_{F+1}\mathbf{a}_{F+1} + \mathbf{b}_{F+1}) \quad (2)$$

The correlation regularization, which will be described in the next subsection, is imposed on the network weights in the fusion layer to identify and utilize the relationships between the structure and fluid features. The overall implementation is demonstrated in Fig. 1.

C. Canonical Correlation Analysis Regularization

Require the projections \mathbf{U} and \mathbf{V} to be regarded as adding an extra linear layer on top of $f(\mathbf{X}^s)$ and $g(\mathbf{X}^f)$ respectively, the correlation objective becomes

$$\begin{aligned} & \max_{\mathbf{U}, \mathbf{V}, \mathbf{W}^s, \mathbf{W}^f} \text{corr}(\mathbf{U}^\top f(\mathbf{X}^s; \mathbf{W}^s), \mathbf{V}^\top g(\mathbf{X}^f; \mathbf{W}^f)) \\ & = \max_{\mathbf{U}, \mathbf{V}, \mathbf{W}^s, \mathbf{W}^f} \frac{\mathbf{U}^\top \boldsymbol{\Sigma}_{12} \mathbf{V}}{\sqrt{\mathbf{U}^\top \boldsymbol{\Sigma}_{11} \mathbf{U} \mathbf{V}^\top \boldsymbol{\Sigma}_{22} \mathbf{V}}}. \end{aligned} \quad (3)$$

where $\boldsymbol{\Sigma}_{12}$, $\boldsymbol{\Sigma}_{11}$, and $\boldsymbol{\Sigma}_{22}$ are the cross-covariance and covariance matrices between the projections and the corresponding variables. To formalize the optimization problem for CCA, we seek to maximize the correlation between the projections \mathbf{U} and \mathbf{V} , as well as the cross-covariance matrices between the projections and their respective variables. The constraints imposed ensure that the projections have unit variance and

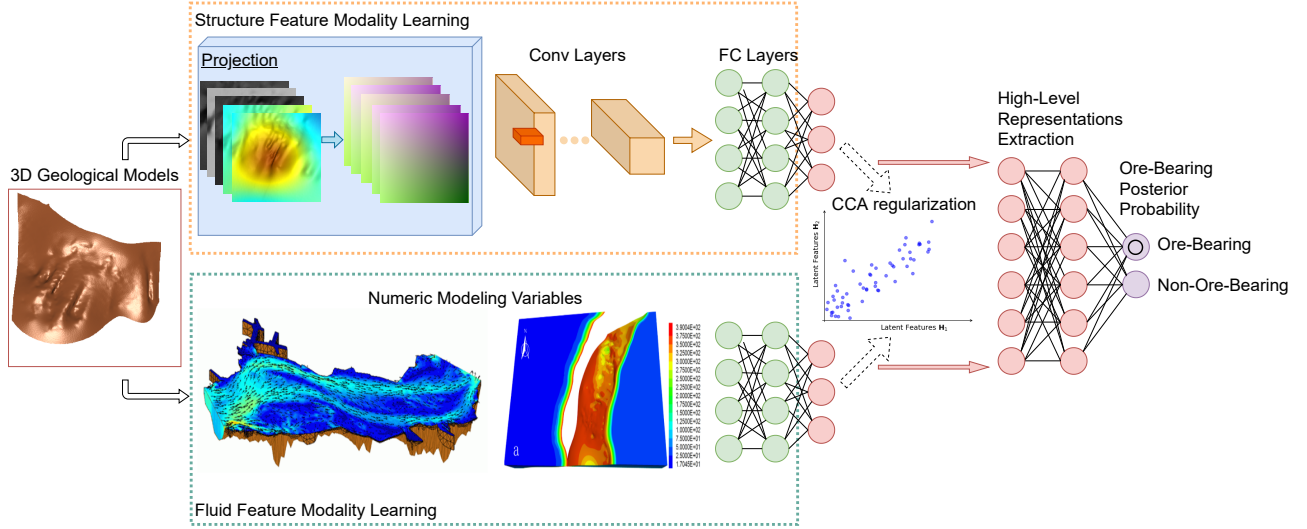


Fig. 1. Schematic of the proposed multimodal learning framework for integrating structure and fluid features.

are orthogonal to each other. Thus we have the constrained optimization problem:

$$\begin{aligned} & \text{Maximize } \text{tr}(\mathbf{U}^\top \boldsymbol{\Sigma}_{12} \mathbf{V}) \\ & \text{s. t. } \mathbf{U}^\top \boldsymbol{\Sigma}_{11} \mathbf{U} = \mathbf{V}^\top \boldsymbol{\Sigma}_{22} \mathbf{V} = \mathbf{I}, \\ & \quad \mathbf{u}_{(i)}^\top \boldsymbol{\Sigma}_{12} \mathbf{v}_{(j)} = 0, \quad \text{for } i \neq j. \end{aligned} \quad (4)$$

We desire to learn multiple projection pairs that are maximally correlated. For simplicity of notation, the final features of the CCA procedure $\mathbf{U}^\top f(\mathbf{X}^s; \mathbf{W}^s)$ and $\mathbf{V}^\top g(\mathbf{X}^f; \mathbf{W}^f)$ with the training set of size N are given as $\mathbf{H}_1 \in \mathbb{R}^{D \times N}$ and $\mathbf{H}_2 \in \mathbb{R}^{D \times N}$, assuming the final layers of two unimodal branches have same output dimension D . We first center \mathbf{H}_1 and \mathbf{H}_2 by subtracting their means:

$$\begin{aligned} \bar{\mathbf{H}}_1 &= \mathbf{H}_1 - \frac{1}{N} \sum_{i=1}^N \mathbf{H}_1 \mathbf{1} \\ \bar{\mathbf{H}}_2 &= \mathbf{H}_2 - \frac{1}{N} \sum_{i=1}^N \mathbf{H}_2 \mathbf{1} \end{aligned} \quad (5)$$

The covariance matrices $\boldsymbol{\Sigma}_{11}$, $\boldsymbol{\Sigma}_{12}$, and $\boldsymbol{\Sigma}_{22}$ are estimated as follows:

$$\begin{aligned} \hat{\boldsymbol{\Sigma}}_{12} &= \frac{1}{N-1} \bar{\mathbf{H}}_1 \bar{\mathbf{H}}_2^\top \\ \hat{\boldsymbol{\Sigma}}_{11} &= \frac{1}{N-1} \bar{\mathbf{H}}_1 \bar{\mathbf{H}}_1^\top + r_1 \mathbf{I}_1 \\ \hat{\boldsymbol{\Sigma}}_{22} &= \frac{1}{N-1} \bar{\mathbf{H}}_2 \bar{\mathbf{H}}_2^\top + r_2 \mathbf{I}_2 \end{aligned} \quad (6)$$

where $r_1, r_2 > 0$ are regularization constants, and \mathbf{I}_1 and \mathbf{I}_2 are identity matrices with dimensions equal to the number of variables in \mathbf{H}_1 and \mathbf{H}_2 , respectively. This setting makes that the covariance matrices $\hat{\boldsymbol{\Sigma}}_{11}$ and $\hat{\boldsymbol{\Sigma}}_{22}$ are invertible to be satisfied in practice because the sample covariance matrices

are estimated from data using regularization. The normalized covariance matrix \mathbf{T} is formed as:

$$\mathbf{T} = \hat{\boldsymbol{\Sigma}}_{11}^{-1/2} \hat{\boldsymbol{\Sigma}}_{12} \hat{\boldsymbol{\Sigma}}_{22}^{-1/2} \quad (7)$$

Next, we compute the SVD of the matrix \mathbf{T} :

$$\mathbf{T} = \mathbf{U} \mathbf{D} \mathbf{V}^\top \quad (8)$$

where \mathbf{U} and \mathbf{V} are the left- and right-singular matrices of \mathbf{T} , and \mathbf{D} denotes a diagonal matrix of singular values. We can then compute the first k left- and right-singular vectors $\mathbf{U}_k = [\mathbf{u}_1, \mathbf{u}_2, \dots, \mathbf{u}_k]$ and $\mathbf{V}_k = [\mathbf{v}_1, \mathbf{v}_2, \dots, \mathbf{v}_k]$, of \mathbf{T} . Finally, the CCA loss is as the negative sum of the top k singular values of \mathbf{T} :

$$\mathcal{L}_{CCA} = - \sum_{i=1}^k \sigma_i, \quad (9)$$

where σ_i is the i -th singular value of \mathbf{T} . The resulting optimal projections are acquired by combining the SVD results with the estimated covariance matrices:

$$(\mathbf{U}^*, \mathbf{V}^*) = \left(\hat{\boldsymbol{\Sigma}}_{11}^{-1/2} \mathbf{U}_k, \hat{\boldsymbol{\Sigma}}_{22}^{-1/2} \mathbf{V}_k \right) \quad (10)$$

D. Model Learning

The loss function for the entire network is a combination of the cross-entropy loss \mathcal{L}_{CE} and CCA regularization, with weights applied to each term:

$$\mathcal{L} = \mathcal{L}_{CE} + \lambda_1 \mathcal{L}_{CCA} + \lambda_2 \sum i^{n_l} \|\mathbf{W}_i\|_F^2 \quad (11)$$

$$\mathcal{L}_{CE} = - \frac{1}{N} \sum_{n=1}^N \left[y_n \log p(\tilde{y}_n | \mathbf{x}_n^s, \mathbf{x}_n^f) + (1 - y_n) \log(1 - p(\tilde{y}_n | \mathbf{x}_n^s, \mathbf{x}_n^f)) \right] \quad (12)$$

where λ_2 is a hyperparameter that controls the strength of the quadratic penalty, n_l is the total number of layers in the network, and \mathbf{W}_i is the weight matrix of the i -th layer. The

$\|\mathbf{W}_i\|_F^2$ term represents the squared Frobenius norm of the weight matrix and encourages smaller values of the network parameters. By minimizing this modified loss function, the network can effectively utilize the relationships between structure and fluid features while also avoiding overfitting.

The gradient of the CCA regularization term with respect to the top-level representations \mathbf{H}_1 and \mathbf{H}_2 can be derived as:

$$\begin{aligned}\nabla_{\mathbf{H}_1} \mathcal{L}_{CCA} &= -\hat{\Sigma}_{11}^{-1/2} \mathbf{U}_k \mathbf{D}^{-1} \mathbf{V}_k^T \hat{\Sigma}_{22}^{-1/2} \hat{\Sigma}_{12}^T \\ \nabla_{\mathbf{H}_2} \mathcal{L}_{CCA} &= -\hat{\Sigma}_{22}^{-1/2} \mathbf{V}_k \mathbf{D}^{-1} \mathbf{U}_k^T \hat{\Sigma}_{11}^{-1/2} \hat{\Sigma}_{12}^T\end{aligned}\quad (13)$$

The gradient with respect to the unimodal branches can be obtained by backpropagating the gradient through the CCA layer and then through the corresponding branch. Let \mathbf{W}_i denote the weight matrix of the i -th layer, and let \mathbf{b}_i denote the bias vector. The computation of the gradient for the weights and biases of the unimodal branches can be achieved as:

$$\begin{aligned}\nabla_{\mathbf{W}_i} \mathcal{L} &= \nabla_{\mathbf{W}_i} \mathcal{L}_{CE} + \lambda_2 \mathbf{W}_i \\ \nabla_{\mathbf{b}_i} \mathcal{L} &= \nabla_{\mathbf{b}_i} \mathcal{L}_{CE}\end{aligned}\quad (14)$$

where $\nabla_{\mathbf{W}_i} \mathcal{L}_{CE}$ and $\nabla_{\mathbf{b}_i} \mathcal{L}_{CE}$ represent the gradients of the cross-entropy loss with respect to the weights \mathbf{W}_i and biases \mathbf{b}_i of the i -th layer, respectively. The term $\lambda_2 \mathbf{W}_i$ adds a regularization term to the gradient to control the magnitude of the weights during training.

Similarly, the gradient with respect to the weights and biases of the CCA regularization can be computed as follows:

$$\begin{aligned}\nabla_{\mathbf{W}^s} \mathcal{L} &= \nabla_{\mathbf{H}_1} \mathcal{L}_{CCA} \cdot \nabla_{\mathbf{W}^s} f(\mathbf{X}^s; \mathbf{W}^s) \\ \nabla_{\mathbf{W}^f} \mathcal{L} &= \nabla_{\mathbf{H}_2} \mathcal{L}_{CCA} \cdot \nabla_{\mathbf{W}^f} g(\mathbf{X}^f; \mathbf{W}^f) \\ \nabla_{\mathbf{U}} \mathcal{L} &= \nabla_{\mathbf{H}_1} \mathcal{L}_{CCA} \cdot f(\mathbf{X}^s; \mathbf{W}^s)^T \\ \nabla_{\mathbf{V}} \mathcal{L} &= \nabla_{\mathbf{H}_2} \mathcal{L}_{CCA} \cdot g(\mathbf{X}^f; \mathbf{W}^f)^T\end{aligned}\quad (15)$$

where \cdot denotes the element-wise multiplication.

Finally, the gradients can be used to update the network parameters using an optimizer, such as stochastic gradient descent (SGD).

IV. STUDY AREA

A. Geological Setting

The Jiaojia gold deposit is located in the Jiaodong Peninsula, which is part of the eastern North China Craton (NCC). The NCC has been the focus of many geological and geophysical studies due to its unique tectonic history and diverse mineral resources. The Jiaodong Peninsula is a major gold-producing region in China, accounting for over 25% of the country's total gold production. The Jiaojia gold deposit is one of the largest and highest-grade gold deposits in the region, with proven reserves of over 100 tons of gold (Fig. 2).

The Jiaojia deposit is hosted by the Jiaodong Group, a Late Archean to Early Paleoproterozoic volcanic-sedimentary sequence, which was intruded by Early Cretaceous granitic rocks. The gold mineralization is closely associated with NNE-trending structures, including the Zhaoping, Jiaojia, and Sanshandao faults. These structures are part of a regional scale,

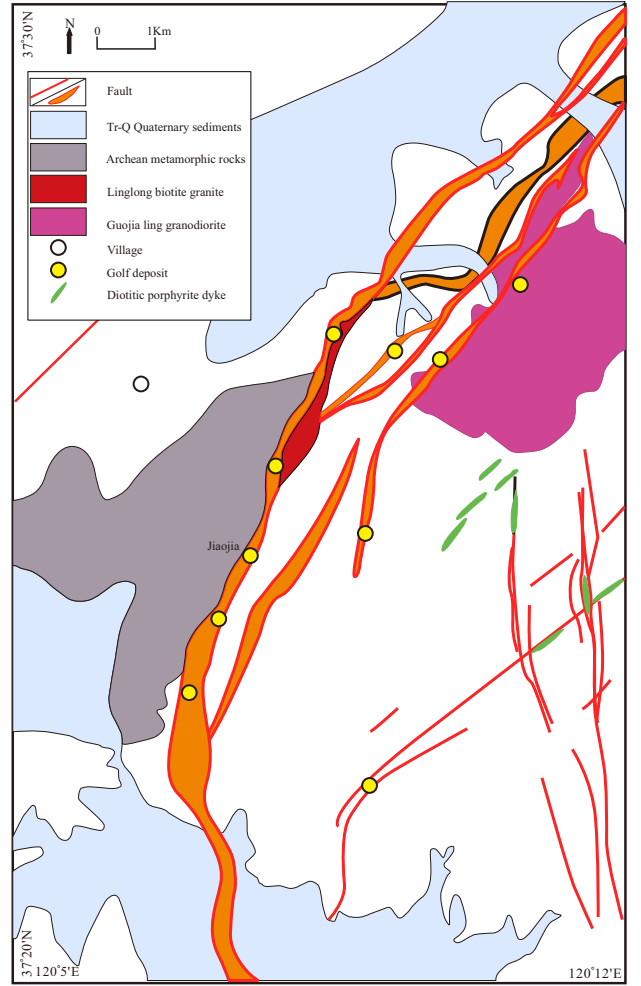


Fig. 2. Geological map of the Jiaojia gold deposit (adapted from [31]).

sinistral strike-slip fault system, which was formed during the Early Cretaceous as a result of the subduction of the Pacific Plate beneath the NCC (Fig. 3).

The gold mineralization at Jiaojia is characterized by multiple stages of quartz veining, brecciation, and alteration, which are closely associated with the NNE-trending faults. The ore bodies are mainly hosted by quartz veins, and the gold mineralization is commonly associated with pyrite, chalcopyrite, and other sulfides. The gold deposits in Jiaodong Peninsula are unique and differ from typical orogenic gold deposits at convergent plate margins, as the geodynamic engine of the Jiaodong gold deposits is the lithospheric thinning and structure adjustment induced by Pacific slab subduction. Thus, the Jiaojia deposit represents an important case study for understanding the tectonic and mineralization processes in the Jiaodong region.

B. Data Preparation

To conduct the multimodal fusion learning for predicting mineral prospectivity in the Jiaojia gold deposit, a current and legacy exploration dataset was collected, including 12 surface maps, 7 subsurface horizontal sections, 226 cross-sections, and

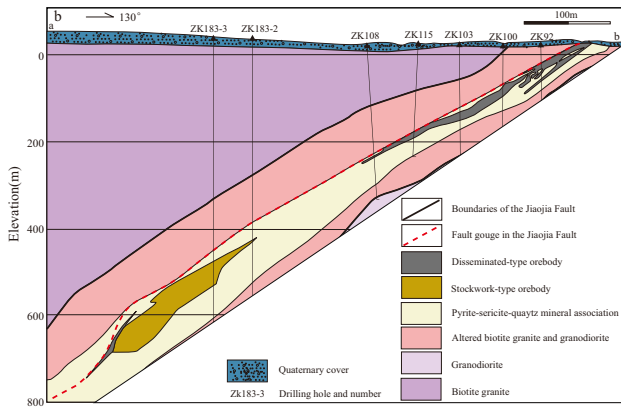


Fig. 3. Mineralization-alteration zoning pattern (at section line # 183) of the Jiaojia gold deposit (adapted from [31]).

779 drillholes (until June 2020). The GIS database for Jiaojia gold deposit was developed by digitizing the cross-section profiles, drillhole data, and associated gold assay data.

From the GIS database, 3D models of the deposit and its geological features were developed using structural data. The shape of the Jiaojia fault was delineated following the cross-section profiles, and the implicit modeling method was used to interpolate the geometry between the delineated contours. The resulting 3D model of the Jiaojia fault was generated from the implicit surface. Voxel models representing the gold distribution were built based on the 3D models of the orebodies, where the 3D area of Jiaojia was divided into regular voxels, each with a size of 25 m x 25 m x 25 m. The kriging method was utilized to interpolate the gold grades for these voxels in terms of Au assay samples. To provide a visual representation of these models, we have included Fig. 4, showcasing the 3D models of Jiaojia deposit.

In addition, fluid data was also extracted to represent the 3D distribution of fluid flow properties. Using FISH output, we obtained the simulation results of volume strain, shear strain, temperature, and Darcy flux from the FLAC3D numerical simulation model. We then developed a workflow to combine the numerical simulation results with the mineralization information into a unified dataset. The dataset has a data structure consistent with the aforementioned mineralization control information, enabling convenient visualization analysis of the numerical simulation results and providing a standard dataset for subsequent mineralization prediction. In this dataset, the simulation results of volume strain and shear strain, temperature gradient, and Darcy flux are respectively used to characterize the connection between tectonic stress, heat, fluid flow, and mineralization.

The resulting samples were labeled as ore-bearing or non-ore-bearing based on the cutoff grade of 1.0 g/t gold, with 17,526 voxels labeled as ore-bearing and the remaining 58,407 voxels labeled as non-ore-bearing. This combined dataset of structural and fluid data was used as input for the multimodal fusion learning approach to predict the mineral prospectivity of the Jiaojia gold deposit.

V. EXPERIMENTS AND RESULTS

A. Prospectivity Modeling

To evaluate the effectiveness of the proposed multimodal fusion learning approach, we applied it to predict mineral prospectivity in the Jiaojia gold deposit. We randomly divided both datasets into training and testing sets in an 8:2 ratio. The training set was used to train the deep learning models, and the testing set was used to evaluate the performance of the models.

To represent the geological features of the deposit, we extracted two types of features from the 3D models: structural and fluid data. The structure features that are extracted from the 3D model include the shape descriptors and surface distance to each voxel [13], [15]. The shape descriptors are calculated using the first 21 Laplace-Beltrami eigenfunctions with non-zero eigenvalues, which encode the intrinsic shape of the Jiaojia fault. These descriptors, together with surface normals, are used to form a 24-channel image that is projected onto each target voxel (Fig. 5). The surface distance is a measure of the distance from the voxel to the surface of the model. This information is used to create a single-channel image that is also projected onto each target voxel (Fig. 6). Together, the 24-channel image and the single-channel image form the structural data that is used as input for the CNN branch of multimodal fusion model.

To combine the numerical simulation results with the mineralization information, we used a custom-built inverse distance weighting interpolation code to interpolate the simulation data points within the spatial domain. The resulting dataset contains unit volume data points throughout the study area that can be matched with known mineralization bodies to obtain a dataset with both numerical simulation results and known mineralization information (Fig. 7).

We used a multilayer perceptron (MLP) [32], [33] to extract the fluid features from the input data, and a convolutional neural network (CNN) to extract the structure features. We also applied a canonical correlation analysis (CCA) regularization to enhance the fusion of the multimodal features. The training process was performed using the Adam optimizer with a learning rate of 1×10^{-5} . We trained the models for ~ 90 epochs and recorded the model with the best performance on the validation set during the training process. For CCA, the regularization parameters r_1/r_2 are selected via grid search. At the top of the multimodal fusion neural network, the feature mappings of two branches are implemented by hidden layers, both reducing dimensions to 256 units for the fusing step. The CCA regularization is utilized on the fusion layer before feature concatenating. We monitor the indicators on the validation set for early stopping. The prospectivity maps were generated using the trained models and evaluated using receiver operating characteristic (ROC) and success rate.

B. Comparisons

We compare the performance of our proposed multimodal fusion model with several other variants (Table I). we compare

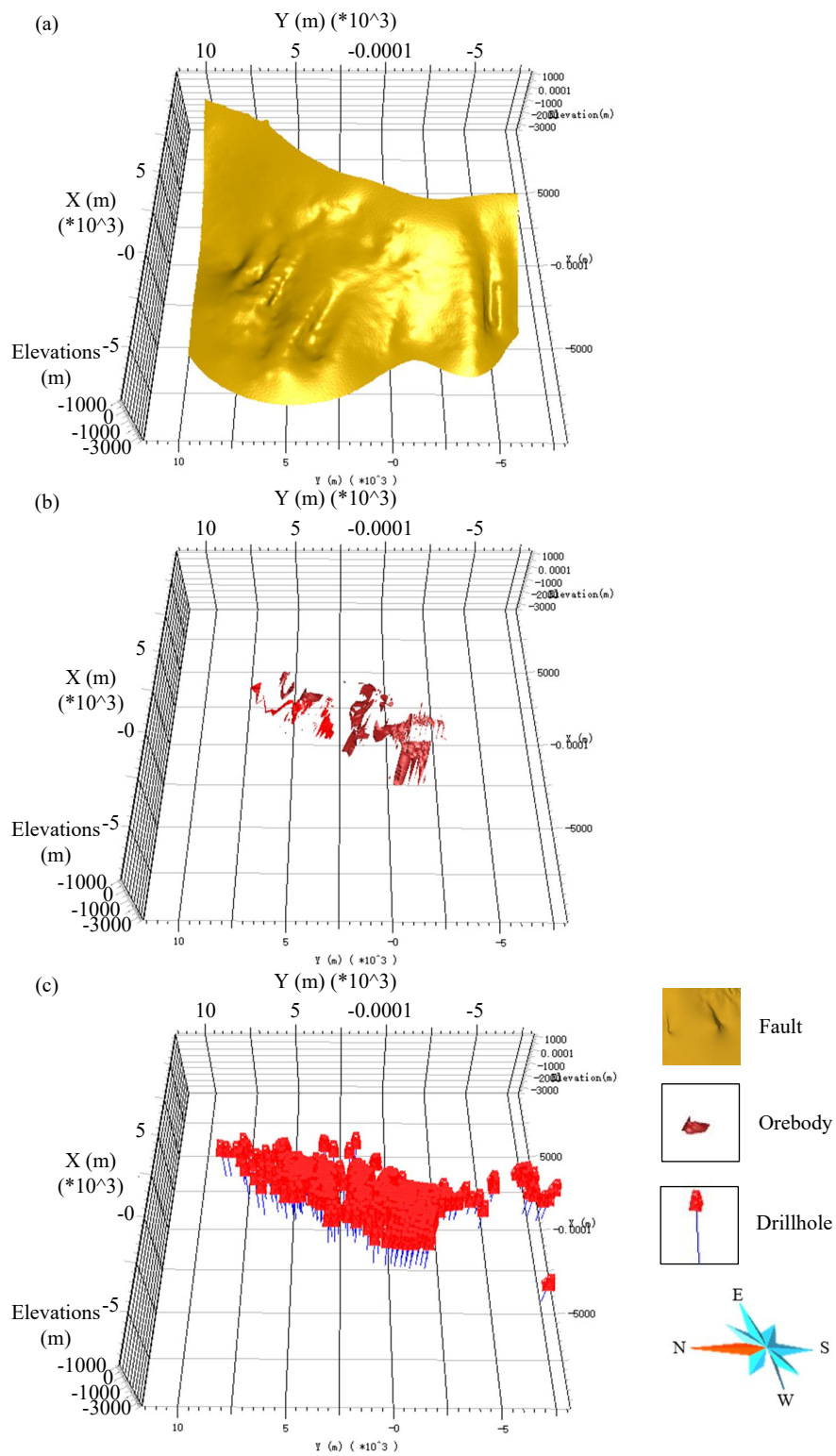


Fig. 4. 3D models of Jiaojia faults (a), orebodies (Au grade $\geq 1\text{g/t}$) (b), and drillholes (c).

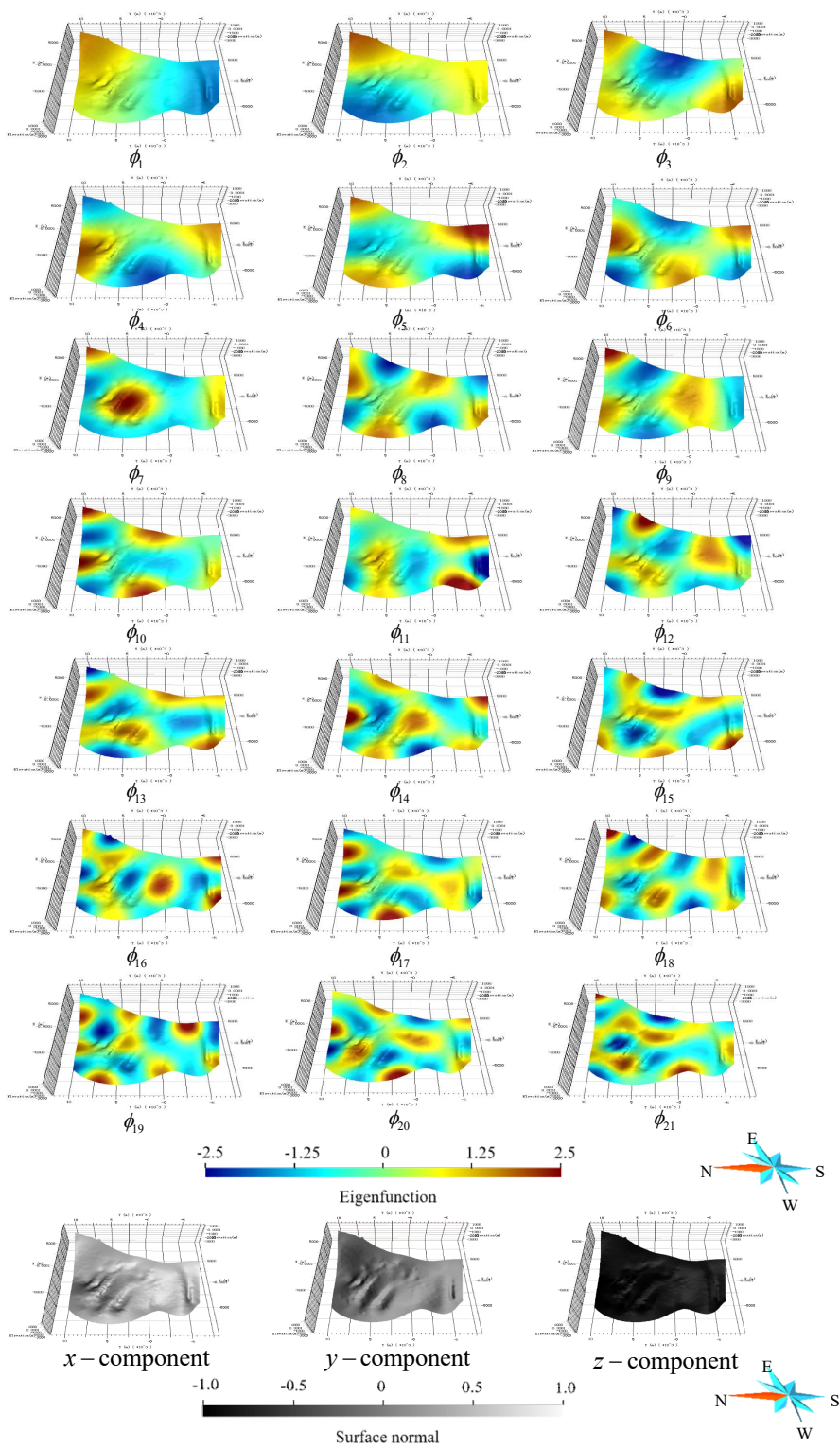


Fig. 5. Shape descriptors of the Jiaoja fault.

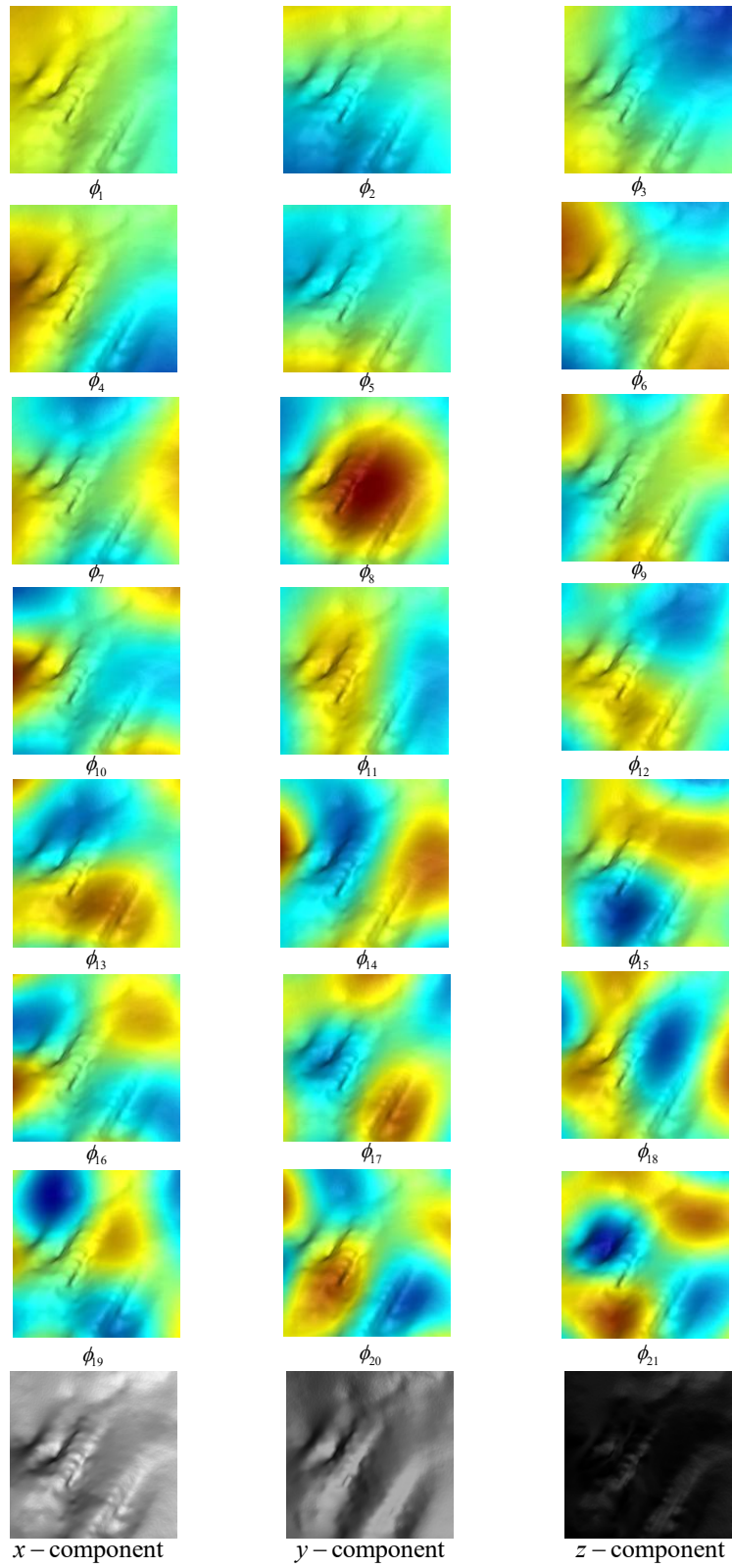


Fig. 6. Projection results of the shape descriptors for target voxels.

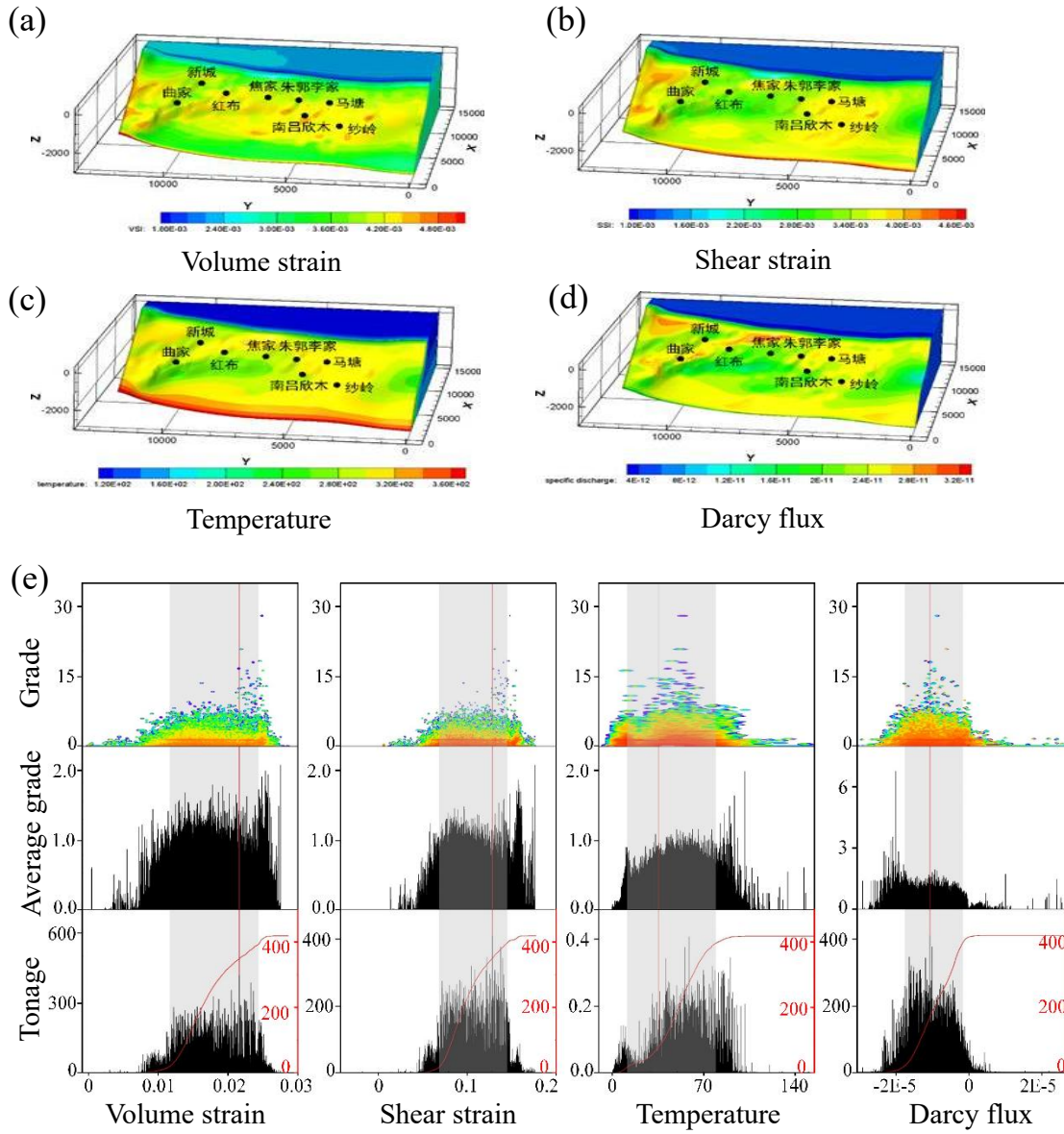


Fig. 7. Simulation results of metallogenic dynamics in Jiaojia deposit (a-d) and association with mineralization (e).

TABLE I
COMPARISON OF METHODS

Comparable Methods	Description
CNN	CNN model utilizing only structure information
(Structure Info Only)	
MLP	MLP model utilizing only fluid information
(Fluid Info Only)	
Prediction with CNN	Prediction using CNN model for structure information
(Structure Info Only)	
Prediction with MLP	Prediction using MLP model for fluid information
(Fluid Info Only)	
Ablation Studies	Description
MLP (All)	MLP model using both structure and fluid information
MLP (All) + CCA	MLP model incorporating CCA to align structural and fluid features
CNN + MLP	Model combining CNN-extracted structure information and MLP-analyzed fluid information
Multimodal Fusion	Proposed model integrating structure and fluid information using CCA

with CNN for structure information only, which only uses a CNN to process structure features mentioned in section V-A. Plus, we compare with MLP for fluid information only, which only uses an MLP to process fluid information. MLPs are statistical learning-based methods and rely on the selection and engineering of appropriate predictor variables to capture the relevant information, which focuses on learning the correlation between hand-crafted predictor variables and mineralization. The predictor variables utilized in the structure feature extraction branch of MLP are consistent with those employed in [13]. These include the structural attributes of voxel models, such as distance to faults, 1st-order/2nd-order undulation, slope and dipping variation of faults, and thickness of the Alteration zone. We include MLP for fluid information only as a baseline, which is placed at the bottom of the comparisons, followed by CNN for structure information only.

In addition to the previously mentioned models, we also compare the performance of CNN+MLP with our proposed multimodal fusion model that incorporates CCA, so that we can assess the effectiveness of incorporating CCA in improving the predictive performance.

To further evaluate the predictive performance of our proposed multimodal fusion model, we conducted two other experiments: prediction with CNN for structural information only and prediction with MLP for fluid information only. These models focus on capturing specific modalities of the data and allow us to assess the individual contributions of structural and fluid information to the prediction task. During the training phase, we leverage both branches to learn representations from the multiple modalities present in the data. While during testing, predictions are made based solely on the structural (fluid) modality, without incorporating any fluid (structural) information. By leveraging the complementary nature of structural and fluid information through multimodal fusion, we can potentially uncover hidden relationships and gain a more comprehensive understanding of the factors influencing mineral prospectivity.

As part of our ablation studies, we aimed to evaluate the influence of dataset variations and network architectures on training (Table I (below)). This assessment offers insights into the advantages of integrating structural and fluid information during modeling. To achieve this, we compared our approach with MLP (all), a model that solely employs MLPs to process both structural and fluid information. Additionally, we compared MLP (all)+CCA, which is similar to MLP (all) but incorporates CCA to align the feature spaces of the structural and fluid MLPs. Another model we compared is CNN + MLP, which combines the structural information extracted by CNN with the fluid information analyzed by MLP. The two branches are integrated to capture the joint effects of structural and fluid properties on mineral prospectivity. By comparing the performance of CNN+MLP with our multimodal fusion model incorporating CCA, we can assess the effectiveness of incorporating CCA in improving predictive performance.

C. Performance Evaluation

We assess the effectiveness of the prospectivity models by analyzing their ROC curves [34] and success-rate curves [35]. The ROC curves indicate how well the models can distinguish between positive and negative instances. We analyze the patterns of the ROC curves for different models to evaluate their performance, and consider the area under the curve (AUC) as a summary measure of the models' overall performance (Fig. 8(a)). The success-rate curves provide insights into the percentage of ore-bearing voxels targeted with respect to all predicted voxels at different thresholds (Fig. 8(b)).

It is notable that both the ROC curves and success rate curves exhibit similar trends. Firstly, the multimodal fusion network demonstrates the highest performance, underscoring its capability to effectively integrate structural and fluid data for mineral prospectivity modeling. It also achieves the highest AUC (0.91) and needs the least areas to cover all ore-bearing voxels. Secondly, Models incorporating CCA, such as MLP (all) + CCA and multimodal fusion + CCA, outperform those without CCA, especially the CNN + MLP model without CCA, suggesting that CCA effectively aligns the feature spaces of structural and fluid data, identifying common patterns and relationships crucial to mineralization. Lastly, the fusion of both modalities consistently outperforms single-modality approaches, regardless of the inclusion of CCA. This emphasizes the significance and efficacy of integrating multi-factor information, including structural and fluid data, in the context of mineral prospectivity modeling.

D. Model Analysis

To assess the joint effects of structural and fluid properties on mineral prospectivity, we evaluate the canonical correlation and the empirical risk (cross-entropy) of the testing samples for the four leading models: MLP (all), MLP (all) + CCA, CNN + MLP, and multimodal fusion. Fig. 9 illustrates the outcomes of canonical correlation and cross-entropy data.

In our analysis, we observed that the multimodal fusion model exhibited the highest canonical correlation among the four models, indicating a strong alignment between the structural and fluid properties. This suggests that the multimodal fusion model effectively captures the joint effects of these modalities in predicting mineral prospectivity.

Regarding the empirical risk, we found that the multimodal fusion model achieved the lowest cross-entropy value, indicating a better fit to the training data and a higher likelihood of accurate predictions on unseen samples.

Overall, our analysis of the canonical correlation and empirical risk suggests that the multimodal fusion model, exhibit stronger joint effects and better predictive performance in capturing the underlying patterns and relationships in the data. This highlights the importance of leveraging both structural and fluid properties and incorporating CCA in improving the accuracy of mineral prospectivity predictions.

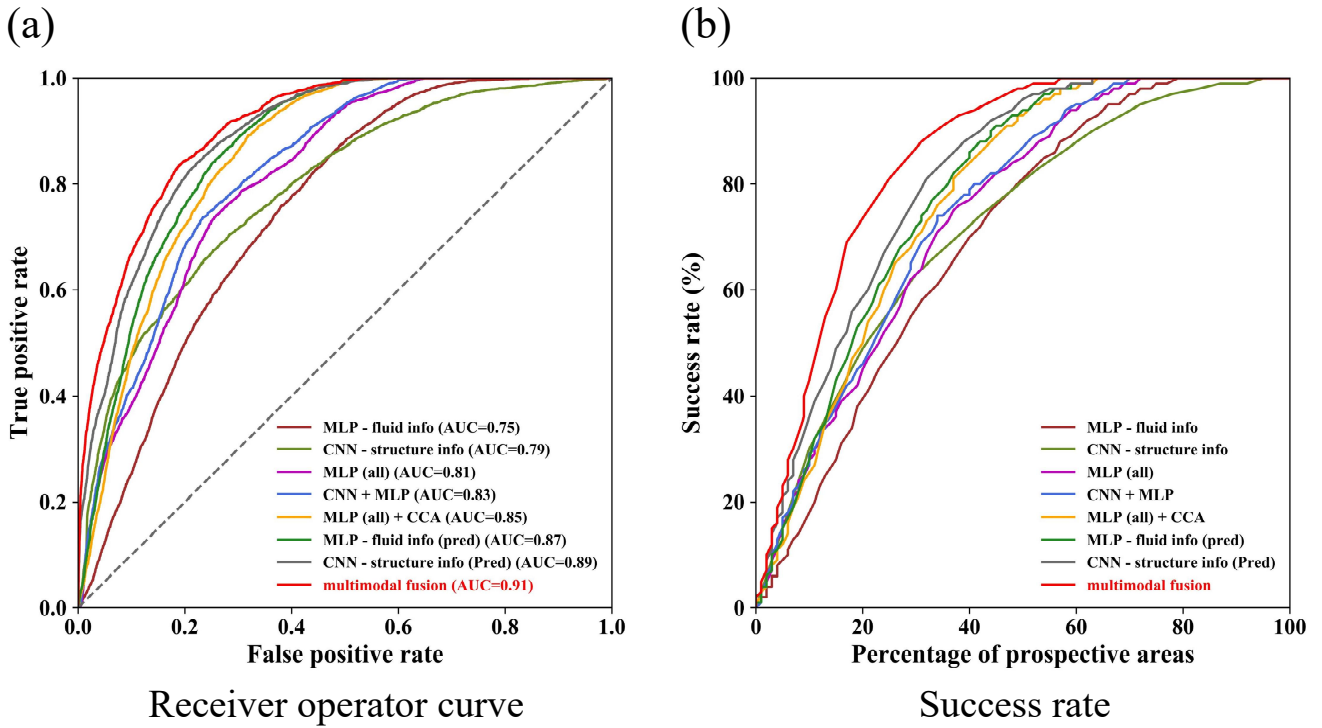


Fig. 8. ROC curves (a) and success-rate curves (b) for the eight evaluated prospectivity models. The multimodal fusion model attains the best performance among the tested methods.

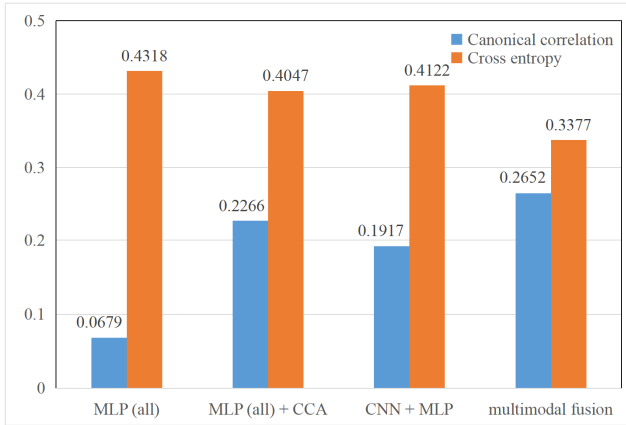


Fig. 9. Canonical correlation and cross-entropy resulting from MLP (all), MLP (all) + CCA, CNN + MLP, and multimodal fusion models.

E. Predictive Mapping and Target Appraisal

An optimal threshold of probability is crucial to distinguish high-probability areas from the low-probability background. To determine this threshold, we follow the approach used in previous studies such as [13], [36]. The probability value that corresponds to the maximum Youden index (MYI) is chosen as the threshold. The MYI, proposed by [37] and further refined by [38], is a metric that maximizes the trade-off between sensitivity and specificity, providing an optimal balance for

classification.

Table II presents the MYIs and their corresponding probability thresholds for the multimodal fusion model and other comparable models. The multimodal fusion model achieves the highest MYI value of 0.6406, indicating its ability to effectively separate high-probability areas from the background, which is consistent with the results of ROC and success rate curves. The corresponding probability thresholds for given prediction models are all higher than the prior probability (0.2374) of ore-bearing voxels.

Fig. 10 shows the high-prospective areas identified by the four prospectivity models. The predictive areas resulting from the multimodal fusion model focus on several potential exploration targets. The fact that the predictive areas resulting from the multimodal fusion model overlap with the high-prospective areas from the other three models, especially the prediction with CNN for structural information-only model, indicates a degree of agreement and consistency among the models in identifying potential exploration targets. In particular, the structural information captured by the CNN branch plays a significant role in determining the high-prospective areas, which are able to detect patterns and spatial relationships that are indicative of mineralization potential. The multimodal fusion model combines both structural and fluid information, leveraging the complementary nature of these modalities to enhance predictive performance. The fact that the resulting predictive areas from the multimodal fusion model align with

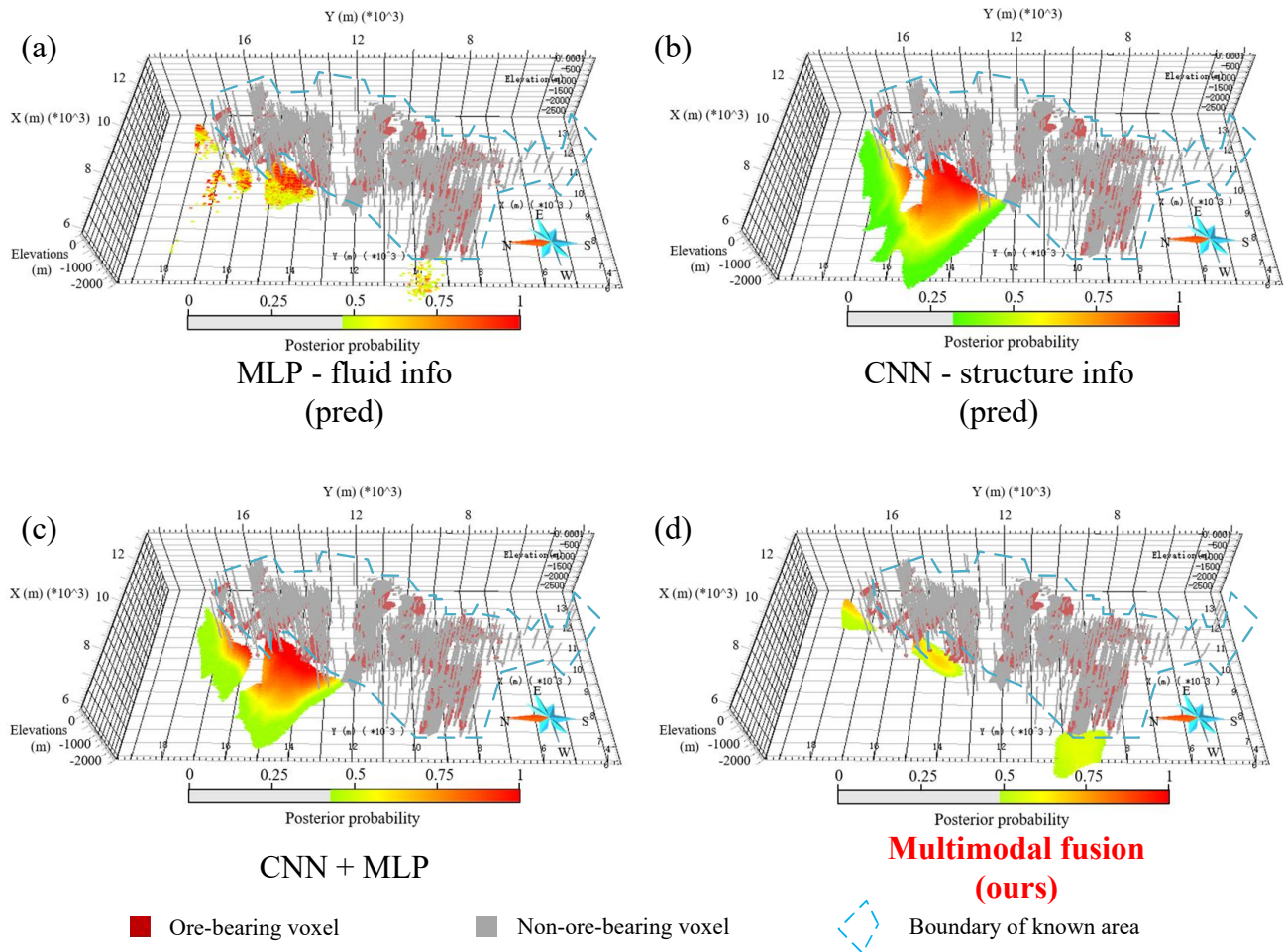


Fig. 10. The high-probability areas resulting from MLP - fluid info (pred) (a), CNN - structure info (pred) (b), CNN + MLP (c) and multimodal fusion (d) models.

the high-prospective areas from the CNN model indicates that the integration of fluid information further reinforces the predictions based on structural information. On the other hand, the overlapping areas between the multimodal fusion model and the prediction with CNN for structural information-only model provide additional confidence in the identified exploration targets.

Based on the predictive results of the multimodal fusion model, three mineral exploration targets have been delineated in the deep-seated areas of the Jiaojia gold deposit. These potential areas, as shown in Fig. 11, exhibit distinct characteristics and high mineralization potential. Target I is located at the intersection of the known shallow mineralization zone, showing favorable structure features and a promising morphology. Target II extends on the southwest side of the main Jiaojia gold deposit and is controlled by significant structural variations, indicating substantial mineralization potential. Target III is connected to the known mineralization zone and exhibits a consistent dip pattern, suggesting an extension of the known mineralization. These delineated potential areas provide valuable guidance for future exploration activities and

TABLE II
MYIS AND THE CORRESPONDING THRESHOLDS FOR THE MULTIMODAL FUSION AND OTHER COMPARABLE MODELS.

Prospectivity model	MYI	Probability
MLP - fluid info (pred)	0.581	0.3387
CNN - structure info (pred)	0.6123	0.478
CNN + MLP	0.499	0.4157
multimodal fusion	0.6406	0.4882

highlight areas of interest for further resource evaluation and development.

VI. CONCLUSIONS

In this study, we propose a multimodal fusion model that combines structural and fluid information for mineral prospectivity modeling. The fusion of multimodal features is achieved by deep networks combining CNN and MLP. Specifically, the canonical correlation analysis is leveraged to guide the alignment of multimodal features. This leads to an effective fusion of structural and fluid information and learns cross-modal features that combine the strength of both modalities

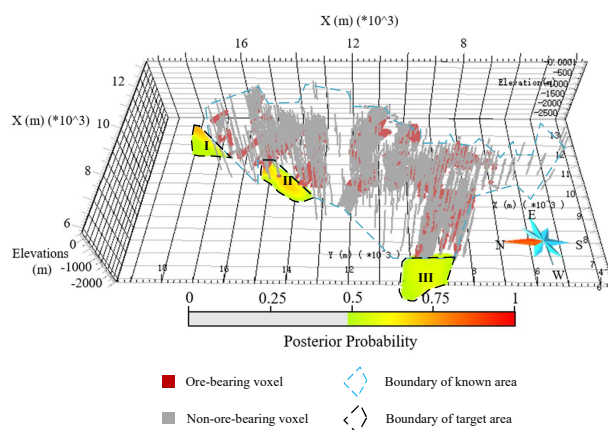


Fig. 11. Three mineral exploration targets identified by the multimodal fusion model.

for prospectivity modeling. Our experimental results demonstrated the effectiveness of this model in improving prediction accuracy. In future work, we plan to further refine the model and explore the incorporation of self-attention mechanisms, such as Transformer-based networks, to potentially boost its performance. Additionally, we aim to investigate the applicability of this model to other types of mineral deposits. Overall, our research contributes to the field of mineral prospectivity modeling and provides valuable insights for decision-making in mineral exploration.

ACKNOWLEDGMENT

The authors would like to acknowledge the invaluable contributions of the anonymous reviewers, whose insightful suggestions greatly improved the quality of this manuscript. This research has been generously supported by the National Natural Science Foundation of China under Grants No. 41972309, 42272344, 42030809, 42072325, and 72088101, as well as the National Key Research and Development Program of China under Grant No. 2019YFC1805905.

REFERENCES

- [1] G. F. Bonham-Carter, "Geographic information systems for geoscientists-modeling with gis," *Computer methods in the geoscientists*, vol. 13, p. 398, 1994.
- [2] E. J. M. Carranza, *Geochemical anomaly and mineral prospectivity mapping in GIS*. Elsevier, 2008.
- [3] E. J. M. Carranza and A. G. Laborte, "Data-driven predictive mapping of gold prospectivity, baguio district, philippines: Application of random forests algorithm," *Ore Geology Reviews*, vol. 71, pp. 777–787, 2015.
- [4] E. J. M. Carranza and A. G. Laborte, "Random forest predictive modeling of mineral prospectivity with small number of prospects and data with missing values in abra (philippines)," *Computers & Geosciences*, vol. 74, pp. 60–70, 2015.
- [5] G. McKay and J. R. Harris, "Comparison of the data-driven random forests model and a knowledge-driven method for mineral prospectivity mapping: A case study for gold deposits around the huritz group and nueltin suite, nunavut, canada," *Natural Resources Research*, vol. 25, no. 2, pp. 125–143, 2016.
- [6] M. Yousefi and V. Nykänen, "Data-driven logistic-based weighting of geochemical and geological evidence layers in mineral prospectivity mapping," *Journal of Geochemical Exploration*, vol. 164, pp. 94–106, 2016.
- [7] Y. Xiong and R. Zuo, "Gis-based rare events logistic regression for mineral prospectivity mapping," *Computers & Geosciences*, vol. 111, pp. 18–25, 2018.
- [8] J. Harris and E. Grunsky, "Predictive lithological mapping of canada's north using random forest classification applied to geophysical and geochemical data," *Computers & Geosciences*, vol. 80, pp. 9–25, 2015.
- [9] A. M. Eldosouky, M. Abdelkareem, and S. O. Elkhateeb, "Integration of remote sensing and aeromagnetic data for mapping structural features and hydrothermal alteration zones in wadi allaqi area, south eastern desert of egypt," *Journal of African Earth Sciences*, vol. 130, pp. 28–37, 2017.
- [10] A. A. Othman and R. Gloaguen, "Integration of spectral, spatial and morphometric data into lithological mapping: A comparison of different machine learning algorithms in the kurdistan region, ne iraq," *Journal of Asian Earth Sciences*, vol. 146, pp. 90–102, 2017.
- [11] Z. Wang, R. Zuo, and L. Jing, "Fusion of geochemical and remote-sensing data for lithological mapping using random forest metric learning," *Mathematical Geosciences*, vol. 53, pp. 1125–1145, 2021.
- [12] Z. Wang, R. Zuo, and H. Liu, "Lithological mapping based on fully convolutional network and multi-source geological data," *Remote Sensing*, vol. 13, no. 23, 2021.
- [13] H. Deng, Y. Zheng, J. Chen, S. Yu, K. Xiao, and X. Mao, "Learning 3d mineral prospectivity from 3d geological models using convolutional neural networks: Application to a structure-controlled hydrothermal gold deposit," *Computers & Geosciences*, vol. 161, p. 105074, 2022.
- [14] S. Bai and J. Zhao, "A new strategy to fuse remote sensing data and geochemical data with different machine learning methods," *Remote Sensing*, vol. 15, no. 4, p. 930, 2023.
- [15] Y. Zheng, H. Deng, J. Wu, R. Wang, Z. Liu, L. Wu, X. Mao, and J. Chen, "Space-associated domain adaptation for three-dimensional mineral prospectivity modeling," *International Journal of Digital Earth*, vol. 16, no. 1, pp. 2885–2911, 2023.
- [16] T. Cui, J. Yang, and I. M. Samson, "Tectonic deformation and fluid flow: implications for the formation of unconformity-related uranium deposits," *Economic Geology*, vol. 107, no. 1, pp. 147–163, 2012.
- [17] Z. Li, G. Chi, K. M. Bethune, K. Eldursi, D. Thomas, D. Quirt, and P. Ledru, "Synchronous egress and ingress fluid flow related to compressional reactivation of basement faults: the phoenix and gryphon uranium deposits, southeastern athabasca basin, saskatchewan, canada," *Mineralium Deposita*, vol. 53, pp. 277–292, 2018.
- [18] Z. Li, G. Chi, K. M. Bethune, K. Eldursi, D. Quirt, P. Ledru, and D. Thomas, "Interplay between thermal convection and compressional fault reactivation in the formation of unconformity-related uranium deposits," *Mineralium Deposita*, vol. 56, pp. 1389–1404, 2021.
- [19] G. Chi, D. Xu, C. Xue, Z. Li, P. Ledru, T. Deng, Y. Wang, and H. Song, "Hydrodynamic links between shallow and deep mineralization systems and implications for deep mineral exploration," *Acta Geologica Sinica-English Edition*, vol. 96, no. 1, pp. 1–25, 2022.
- [20] M. Rabiei, G. Chi, E. G. Potter, D. C. Petts, F. Wang, and R. Feng, "Spatial variations in fluid composition along structures hosting unconformity-related uranium deposits in the athabasca basin, canada:

- implications for ore-controlling factors,” *Mineralium Deposita*, pp. 1–25, 2023.
- [21] S. Li, B.-m. Jahn, S. Zhao, L. Dai, X. Li, Y. Suo, L. Guo, Y. Wang, X. Liu, H. Lan, *et al.*, “Triassic southeastward subduction of north china block to south china block: Insights from new geological, geophysical and geochemical data,” *Earth-Science Reviews*, vol. 166, pp. 270–285, 2017.
- [22] Z. Ziyong, Y. Hangyu, and G. Xiaodan, “Fuzzy fusion of geological and geophysical data for mapping hydrocarbon potential based on gis,” *Petroleum Geoscience*, vol. 24, no. 1, pp. 131–141, 2018.
- [23] H. K. Olierook, R. Scalzo, D. Kohn, R. Chandra, E. Farahbakhsh, C. Clark, S. M. Reddy, and R. D. Müller, “Bayesian geological and geophysical data fusion for the construction and uncertainty quantification of 3d geological models,” *Geoscience Frontiers*, vol. 12, no. 1, pp. 479–493, 2021.
- [24] M. J. Cracknell and A. M. Reading, “Geological mapping using remote sensing data: A comparison of five machine learning algorithms, their response to variations in the spatial distribution of training data and the use of explicit spatial information,” *Computers & Geosciences*, vol. 63, pp. 22–33, 2014.
- [25] D. R. Hardoon, S. Szedmak, and J. Shawe-Taylor, “Canonical correlation analysis: An overview with application to learning methods,” *Neural computation*, vol. 16, no. 12, pp. 2639–2664, 2004.
- [26] H. Hotelling, “Relations between two sets of variates,” *Biometrika*, vol. 28, no. 3/4, pp. 321–377, 1936.
- [27] G. Andrew, R. Arora, J. Bilmes, and K. Livescu, “Deep canonical correlation analysis,” in *International conference on machine learning*, pp. 1247–1255, PMLR, 2013.
- [28] W. Wang, R. Arora, K. Livescu, and J. A. Bilmes, “Unsupervised learning of acoustic features via deep canonical correlation analysis,” in *2015 IEEE International Conference on Acoustics, Speech and Signal Processing (ICASSP)*, pp. 4590–4594, IEEE, 2015.
- [29] M. Raghu, J. Gilmer, J. Yosinski, and J. Sohl-Dickstein, “Svcca: Singular vector canonical correlation analysis for deep learning dynamics and interpretability,” *Advances in neural information processing systems*, vol. 30, 2017.
- [30] Y. Zhong, C.-Y. Wu, S. You, and U. Neumann, “Deep rgb-d canonical correlation analysis for sparse depth completion,” *Advances in Neural Information Processing Systems*, vol. 32, 2019.
- [31] J. Deng, C. Wang, L. Bagas, E. J. M. Carranza, and Y. Lu, “Cretaceous–cenozoic tectonic history of the jiaojia fault and gold mineralization in the jiaodong peninsula, china: constraints from zircon u–pb, illite k–ar, and apatite fission track thermochronometry,” *Mineralium Deposita*, vol. 50, pp. 987–1006, 2015.
- [32] M. Abedi and G.-H. Norouzi, “Integration of various geophysical data with geological and geochemical data to determine additional drilling for copper exploration,” *Journal of Applied Geophysics*, vol. 83, pp. 35–45, 2012.
- [33] R. Ghezelbash, A. Maghsoudi, and E. J. M. Carranza, “Sensitivity analysis of prospectivity modeling to evidence maps: Enhancing success of targeting for epithermal gold, takab district, nw iran,” *Ore Geology Reviews*, vol. 120, p. 103394, 2020.
- [34] M. Barreno, A. Cardenas, and J. D. Tygar, “Optimal roc curve for a combination of classifiers,” *Advances in Neural Information Processing Systems*, vol. 20, pp. 57–64, 2007.
- [35] F. P. Agterberg and G. F. Bonham-Carter, “Measuring the performance of mineral-potential maps,” *Natural Resources Research*, vol. 14, no. 1, pp. 1–17, 2005.
- [36] Y. Chen and W. Wu, “Mapping mineral prospectivity using an extreme learning machine regression,” *Ore Geology Reviews*, vol. 80, pp. 200–213, 2017.
- [37] W. J. Youden, “Index for rating diagnostic tests,” *Cancer*, vol. 3, no. 1, pp. 32–35, 1950.
- [38] M. D. Ruopp, N. J. Perkins, B. W. Whitcomb, and E. F. Schisterman, “Youden index and optimal cut-point estimated from observations affected by a lower limit of detection,” *Biometrical Journal: Journal of Mathematical Methods in Biosciences*, vol. 50, no. 3, pp. 419–430, 2008.